▌**Lasers** │*Hot Paper*│

How the Physicochemical Properties of the Bulk Material Affect the Ablation Crater Profile, Mass Balance, and Bubble Dynamics During Single-Pulse, Nanosecond Laser Ablation in Water

Mark-Robert Kalus,[a] Stephan Barcikowski,*[a] and Bilal Gökce[a, b]

Abstract: Understanding the key steps that drive the laser-based synthesis of colloids is a prerequisite for learning how to optimize the ablation process in terms of nanoparticle output and functional design of the nanomaterials. Even though many studies focus on cavitation bubble formation using single-pulse ablation conditions, the ablation efficiency and nanoparticle properties are typically investigated under prolonged ablation conditions with repetition rate lasers. Linking single-pulse and multiple-pulse ablation is difficult due to limitations induced by gas formation cross-effects, which occur on longer timescales and depend on the target materials' oxidation-sensitivity. Therefore, this study investigates the ablation and cavitation bubble dynamics under nanosecond, single laser pulse conditions for six different bulk materials (Au, Ag, Cu, Fe, Ti, and Al). Also, the effective threshold fluences, ablation volumes, and penetration depths are quantified for these materials. The thermal and chemical properties of the corresponding bulk materials not only favor the formation of larger spot sizes but also lead to the highest molar ablation efficiencies for low melting materials such as aluminum. Furthermore, the concept of the cavitation bubble growth linked with the oxidation sensitivity of the ablated material is discussed. With this, evidence is provided that intensive chemical reactions occurring during the very early timescale of ablation are significantly enhanced by the bubble collapse.

Introduction

The phenomenon of cavitation is of great importance not only due to its substantial damage potential for hydraulic machines,[1–3] but also for its use in high-pressure homogenizers in the food industry,[4, 5] or its ability to induce sonochemical reactions for water purification.[6–8] Cavitation effects further play an important role in the field of liquid-assisted laser applications, e.g., medical laser applications,[9, 10] laser-micromachining,[11–13] or laser ablation in liquids (LAL).[14] In the latter case, laser pulses are focused onto a bulk target immersed in a liquid, enabling the cost-effective[15] production of colloids on the gram-scale[16, 17] from a wide range of different material classes such as metals,[18–20] oxides[21–23] or alloys[24–28] in different liquids.[29–32] These synthesized nanoparticles typically are of high purity[33] and are promising materials for application fields such as biomedicine,[24, 34] catalysis,[35–38] or 3D printing.[39–43]

Generally, LAL is characterized by different competing physical and chemical phenomena that are determined by the interaction between the laser, the target, and the liquid. After the laser pulse interacts with the bulk target, a high-temperature plasma is generated containing a high density of free electrons and ablated matter.[44] This plasma interacts with the surrounding liquid inducing its phase transition and the formation of an expanding cavitation bubble.[45–47] The elucidation of the cavitation bubble's role in the formation of the nanoparticles (NPs) is a main research topic among researchers working on LAL. A better understanding would allow more precise control of the ablation conditions and thus enable the optimization of the particle properties such as size and composition.

Small-angle X-ray scattering (SAXS) measurements indicated that the cavitation bubble is homogenously filled with both primary and secondary NPs[48–50] while solid, crystalline, secondary particles were also detected at the bubble front.[51] For ultrashort pulse durations at high effective laser fluences, the secondary particles likely originate from Rayleigh instabilities of the molten metal layer, which induce the formation of nano-droplets by thin layer disintegration and jetting from the molten target material.[52] Zhigilei et al. have recently extended their atomistic simulations to ns-pulses to explain the wider

[a] M.-R. Kalus, Prof. Dr. S. Barcikowski, Prof. Dr. B. Gökce
Technical Chemistry I
Center for Nanointegration Duisburg-Essen (CENIDE)
University of Duisburg-Essen
45141 Essen (Germany)
E-mail: stephan.barcikowski@uni-due.de

[b] Prof. Dr. B. Gökce
Materials Science and Additive Manufacturing
School of Mechanical Engineering and Safety Engineering
University of Wuppertal
42119 Wuppertal (Germany)

Chemistry–A European Journal

Full Paper
doi.org/10.1002/chem.202005087

Chemistry Europe
European Chemical
Societies Publishing

particle size distribution for longer laser pulse durations (as opposed to ultrashort pulses, for which bimodality is often observed) and have defined three different NP formation regimes and pathways.[53] Their simulations have further indicated that the liquid in the region between the molten material and the bulk liquid transforms into a supercritical state forming a mixing region containing supercritical water and target vapor, which serves as the initiator for the formation of the cavitation bubble.[53,54] Unfortunately, these simulations have so far not considered chemical reactions between the liquid molecules and the ablated matter. Therefore, theoretical simulations typically assume that the cavitation bubble consists mainly of solvent molecules (target atoms:solvent molecules $\approx$ 1:20).[55]

However, chemical reactions likely take place within the cavitation bubble, as supported by Qiang et al., who observed that the cavitation bubble size is larger for LAL of Al compared to LAL of Cu and LAL of Ti.[56] Furthermore, Reich et al. measured the relative content of unoxidized zinc species during the cavitation bubble evolution for ns-LAL of Zn in water using X-ray absorption spectroscopy.[57] They have shown that during LAL not only nanoparticles but also reactive Zn atoms are formed in the early cavitation bubble stage. The authors observed that the content of the reactive species dropped during bubble expansion and cooling of the interior, but only disappeared with the bubble collapse indicating that reactive atomic or atom cluster species (which are likely to act as particle growth precursors) are present in the cavitation bubble. These observations are supported by Letzel et al., who observed by in situ synchrotron x-ray scattering studies that the addition of small amounts of sodium chloride to water leads to a size quenching of the NPs, providing evidence that size quenching already occurs within the cavitation bubble.[58] The same in situ quenching within the cavitation bubble was observed for small organic molecules, whereas this was not the case for macromolecular ligands.[59]

However, the time regime of the rebound/collapse of the bubble must also be considered but is often neglected as most studies focus on the primary cavitation bubble cycle. Within this context, several studies have demonstrated that water is decomposed during LAL resulting in the formation of molecular hydrogen, oxygen, and hydrogen peroxide.[60–67] The individual formation rates of these decomposition products depend strongly on the type of the ablated material. The ablation of catalytically active materials (e.g., Pt) in water leads to high hydrogen peroxide formation rates. In contrast, the ablation of oxidation-sensitive materials in water produces large amounts of molecular hydrogen.[62,63] The redox chemistry between the target material and water affects not only the NP productivity during long-term ablation but also the oxidation degree of the final NPs, as also theoretically predicted by Reichenberger et al. based on Nernst equation and correlated to experimental findings[35,62,63] However, all these experiments were performed for multi-pulse laser ablation with repetition rates in the kHz regime. Hence, cavitation bubbles,[16,17] persistent bubbles[60–63] or NPs[61–63,68–70] formed during LAL induce cross-effects. Although strategies have been developed to overcome these limitations (e.g., by optimizing the scanning strategy[16,17] and applying liquid flow setups),[17,71] such cross-effects cannot be completely avoided.

Additionally, incubation effects can occur during multi-pulse laser ablation, influencing the cavitation bubble size and ablation yield depending on the number of applied laser pulses, the target material type, and the chosen laser parameters.[72,73] In detail, increasing the number of laser pulses from 1 to 30 at low fluences leads to a steady increase in cavitation bubble volume.[72] In contrast, the cavitation bubble volume and the NP mass concentration within the bubble decrease exponentially for a number of pulses between 100 and 1000.[73] Knowing the concentration of ablated mass within the cavitation bubble volume for a single laser pulse would allow better adjustment of simulation experiments and calibration of in situ SAXS and WAXS (small- and wide-angle X-ray scattering, respectively) studies.

Therefore, an overall question is how the physicochemical properties of the target material and its chemical reactivity with the liquid environment influence the ablation process decoupled from any cross-effects. This study sheds light on these knowledge gaps by investigating the cavitation bubble formation and ablation efficiency for single-pulse nanosecond LAL (SP-ns-LAL) of six different materials (Au, Ag, Cu, Fe, Ti, and Al) in water. In the first part of this work, the ablation craters of each material are characterized by confocal 3D and scanning electron microscopy with respect to their spot diameter, ablation depth, volume, and surface morphology. In the second part, the cavitation bubble dynamics are evaluated depending on the oxidation sensitivity of the ablated target material. In the third part, the amount of ablated matter is correlated to the cavitation bubble dynamics. A mechanistic picture summarizing the physical and chemical parameters determining the ablation process during SP-ns-LAL completes this study.

Experimental Section

Materials

SP-ns-LAL experiments were performed using gold (99.99%, 10×10×1 mm, Allgemeine Gold), silver (99.99%, 10×10×1 mm, GoodFellow), copper (99.99%, 10×10×0.5 mm, GoodFellow), iron (99.98%, 10×10×0.2 mm, GoodFellow), titanium (99.96%, 10×10×0.2 mm, GoodFellow), and aluminum (99.0%, 10×10×1 mm, GoodFellow) substrates for ablation. The experiments were performed in deionized Milli-Q water (18.2 MΩ cm at 25 °C).

Methods

Single-pulse nanosecond laser ablation in liquids (SP-ns-LAL)

SP-ns-LAL was performed in a custom-designed ablation flow chamber (h: 7 mm, w: 20 mm, l: 30 mm) made of acrylonitrile butadiene styrene (ABS) polymer. The internal volume of the chamber was 4.2 cm³. Furthermore, side observation windows made of float glass were integrated into the chamber for the cross-sectional imaging of the cavitation bubbles. Float glass with a thickness of 1.1 mm was also used as an entrance window for the laser beam. The inlet of the ablation chamber was connected via a tube to a syringe pump, which delivered a pulsation-free volumetric flow rate of 5 mL min⁻¹. The time interval between each laser shot was

Chemistry–A European Journal

Full Paper
doi.org/10.1002/chem.202005087

Chemistry Europe
European Chemical
Societies Publishing

set to 3 min to ensure complete fluid exchange in the ablation flow chamber. This way, screening effects induced by the interaction of the laser beam with pre-existing NPs[62,63] or persistent microbubbles[60,62,63] were avoided.

The ablation targets were polished with abrasive paper to remove the native oxide layer that forms on the highly oxidation-sensitive metals' surfaces. Afterward, the ablation targets were ultrasonically rinsed with ethanol for 10 min, dried with argon, and placed in the ablation chamber using a double-sided adhesive tape. The liquid level in the ablation chamber without the ablation target was 6 mm.

For SP-ns-LAL, an Nd:YAG laser (Innolas, Spitlight DPSS250-100) was used, operating with a pulse duration of 9 ns, a wavelength of 1064 nm, and a pulse energy of 30 mJ. The laser beam with a raw beam diameter d_0 of 3 mm was focused on the ablation target through a lens with a focal length of 75 mm, which was screwed onto an optical positioning system. The laser fluence was varied by adjusting the working distance between the ablation target and the focusing lens from −10 mm to 3 mm, as displayed in Figure 1a and b. A negative/positive working distance corresponds to the focus placed into the liquid/behind the target. At a working distance of zero, the focal plane is on the ablation target. The effective spot diameter was determined by confocal 3D microscopy (Nanofocus) for each working distance and material to calculate the effective laser fluence (Figure 1a). Note that for a better illustration of the results the error bars (see Figure S1a in the Supporting Information) are not shown. Additionally, the theoretical, incident spot size was calculated considering the laser beam's refraction at the air-glass-water interfaces (see Table S1 in the Supporting Information for more details). The incident and effective laser fluence was then calculated by dividing the applied pulse energy by the calculated (=incident) or measured (=effective) spot area, respectively, as shown in Figure 1b (the errors can be found in Figure S1b in the Supporting Information). The laser beam was directed to a power meter via a 50/50 beam splitter placed between the laser and the lens to control the pulse energy. Hence, the initial pulse energy of 30 mJ was halved, and a pulse energy of 15 mJ was directed towards the ablation chamber. The effective pulse energy was further corrected from 15 mJ to 11.9 mJ considering the laser beam's attenuation due to reflection at the lens, the ablation window, and the liquid layer above the target. Thus, the effective laser fluences ranged from 21 to 72 J cm^{-2} depending on the target material and the working distance between the lens and the ablation target (Figure 1c) while for the incident laser fluence values ranging from 21 to 313 J cm^{-2} were calculated by theory (see Table S1 in the Supporting Information). Hence, for the 6 investigated metals, at high incident fluences, the effective fluence is only 6 – 24% of the incident fluence during ns LAL. The error bars

were derived by triple-determination (see Figure S1b in the Supporting Information).

Furthermore, the crater depth and volume were determined by confocal 3D microscopy, which allowed the ablation craters' characterization with high lateral and depth resolution of several nanometers. The target surface morphology was measured by scanning electron microscopy (Phillips, XL20). The entire experimental setup and procedure are sketched in Figure 2.

Imaging of the cavitation bubbles

A videography system with a minimum delay time of 53 µs was used to image the cavitation bubbles.[73] With each laser shot, the ablation chamber was moved perpendicular to the laser beam so that the next laser pulse could hit a non-ablated part of the target surface. The cavitation bubble's lifetime was recorded by varying the delay time in steps of 10 µs. By keeping the delay time constant at 80 µs, representing the maximum bubble expansion time, cavitation bubble images were recorded by varying the working distance between the lens and the ablation target. The cavitation bubble size (diameter and height) was determined using ImageJ (version 1.51 s), while the cavitation bubble volume was calculated by assuming a hemispherical bubble geometry (at maximum bubble size).

Results and Discussion

Characterization of the ablation craters depending on the physicochemical properties of the target materials and the laser fluence

During ns-LAL of metals in water, the ablation efficiency is affected by the formation of persistent bubbles, whose formation rates strongly depend on the redox potential of the target material.[62,63] Thus, for batch-wise, multiple-pulse ns-LAL in water, performed for longer time periods than a single laser pulse, the lowest NP productivities are often obtained for very oxidation-sensitive materials such as Ti or Al since a large amount of persistent bubbles form during their ablation, continuously shielding the laser beam and hence, reducing the ablation efficiency during long-term ablation.[16,62,63] Furthermore, shielding effects induced by the NPs reduce ablation efficiency.[61–63,68,69] In this context, the question arises how the ablation process proceeds if no shielding cross-effects are present, and when just the interaction between the laser pulse and the target material in the liquid environment is considered. For this purpose, a single laser pulse with an incident pulse energy of 11.9 mJ (this value refers to the corrected incident pulse energy described in the experimental section) was focused on a
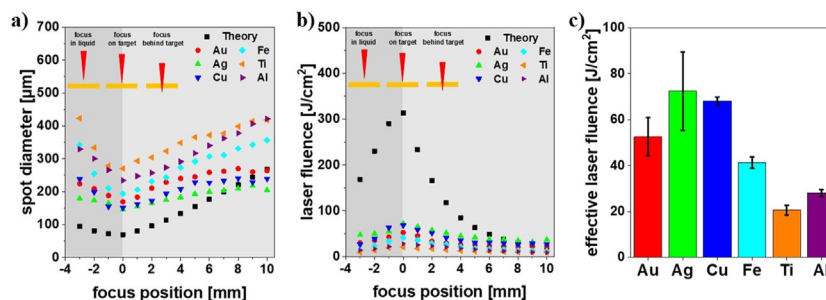

Figure 1. (a) Incident/effective spot diameter and (b) laser fluence as a function of the focus position. (c) Effective laser fluence in the focus position (at a theoretical, incident fluence of 313 J cm^{-2}).

Chemistry–A European Journal

Full Paper
doi.org/10.1002/chem.202005087

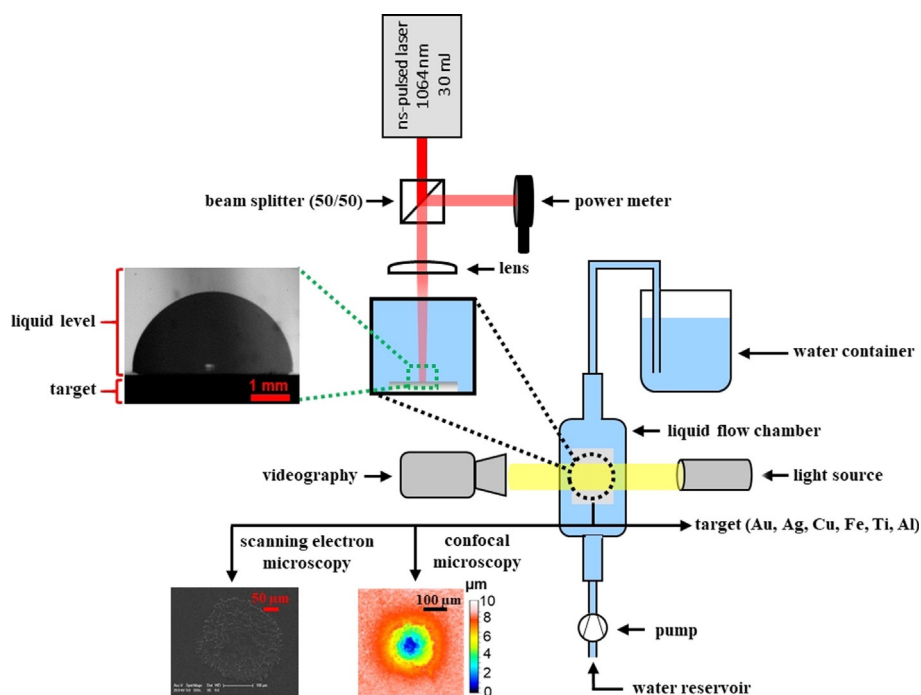**Chemistry Europe**
European Chemical
Societies Publishing

Figure 2. Experimental setup for cross-sectional imaging of cavitation bubbles formed during SP-ns-LAL of Au, Ag, Cu, Fe, Ti, and Al in a liquid flow chamber. The target materials were characterized by confocal 3D and scanning electron microscopy directly after ablation.

bulk target immersed in water. Au, Ag, Cu, Fe, Ti, and Al were selected as bulk materials, covering a wide range of physicochemical properties and redox activities. Consequently, different effective spot sizes were obtained and characterized by confocal 3D microscopy, as displayed in Figure 3a for an exemplary incident laser fluence of 166 $J\,cm^{-2}$. It is evident that the effective spot size strongly depends on the choice of the ablated material. Spot diameters are largest for Fe, Ti, and Al ranging from 300 to 400 µm, whereas it is approximately half for Au, Ag, and Cu. Also, the ablation depth depends on the target material, as illustrated in Figure 3b. SP-ns-LAL of Al yields deepest crater structures with an ablation depth of

9 µm followed by Ag (4 µm), Au (3 µm), Cu and Ti (2 µm), and Fe (1 µm).

Since the ablation rate and the ablation depth depend strongly on the incident laser fluence,[16,17] the experiments were repeated for a broad range of incident laser fluences between 21 and 313 $J\,cm^{-2}$ (Figure 3c–e). The ablation craters are deepest after SP-ns-LAL of Al, whereby the ablation depth increases with increasing incident laser fluence from 3 µm to 9 µm until a threshold fluence of 166 $J\,cm^{-2}$ is reached. A further increase in the incident laser fluence has no further influence on the ablation depth. Also, for Au (0.8 to 2.2 µm), Ag (0.9 to 4.6 µm), and Cu (0.8 to 2.7 µm), the abla-
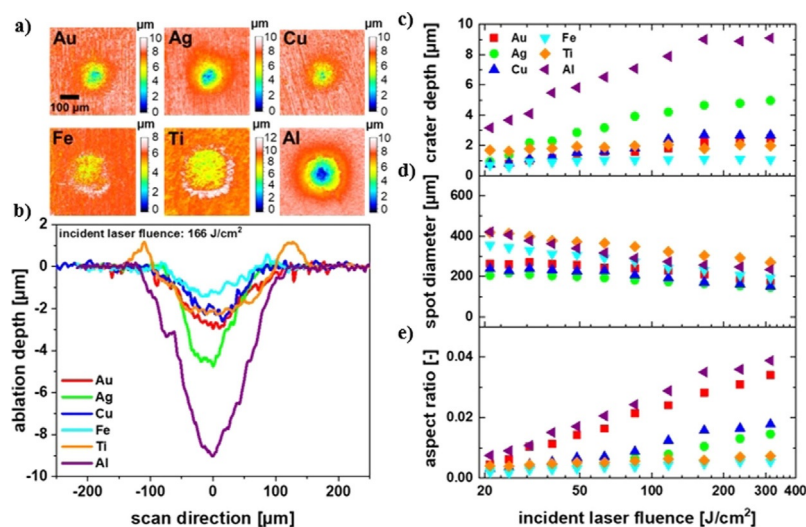
Figure 3. (a) Confocal 3D microscopy images obtained after SP-ns-LAL of Au, Ag, Cu, Fe, Ti, and Al in water with a theoretical, incident laser fluence of 166 $J\,cm^{-2}$. (b) Line scans of these ablation craters. The minimum of the ablation profiles was centred to the zero position. (c–e) Crater depth, spot diameter, and corresponding aspect ratio (crater depth divided by the spot diameter) as a function of the theoretical, incident laser fluence.

tion depth increases with increasing incident laser fluence and saturates above a threshold fluence of 166 J cm^{-2}. The reason for the ablation depth saturation could be attributed to the laser intensities of 2–3.5×10^{10} W cm^{-2}, which are reached in the fluence regime >166 J cm^{-2} and possibly promote the optical breakdown of the liquid. In this context, Docchio et al. found threshold values of 3×10^{10} W cm^{-2} for the optical breakdown in pure water under focusing conditions comparable to the present study.[74] In contrast to Au, Ag, Cu, and Al, the ablation depth changes only slightly for Fe and Ti. Note that the determination of the crater depth for these metals was difficult due to the formation of melting edges, whose height depended strongly on the applied laser fluence (see Figure S2). For this reason, the horizontal along the target surface was used as a reference line, resulting in ablation depths of 0.7 to 1 µm for Fe and 1.7 to 2 µm for Ti. Ouyang et al. observed similar melting edges after ns-LAL of Ti alloys in water accompanied by the formation of waves and cracks on the target surface. They stated that the low thermal conductivity of the ablated metal favors the formation of this surface morphology.[75]

Considering the spot diameters displayed in Figure 3 d, one can observe a steady decrease of the spot diameter with increasing incident fluence due to the tighter focusing of the laser beam. Furthermore, the lateral dimensions of the spot diameters are two orders of magnitude larger than the ablation depth. Consequently, the aspect ratios (crater depth divided by spot diameter) are very low and range from 0.001 to 0.04, following the trend Fe $<$ Ti $<$ Ag $<$ Ag $<$ Cu $\ll$ Au $<$ Al as shown in Figure 3 b,e.

For further discussion, the dependence of the ablation depth on the incident laser fluence was evaluated. Generally, two different ablation regimes are distinguished in ultrashort-pulsed LAL, characterized by a logarithmic dependence of the ablation depth on the laser fluence.[76–79] At low laser fluences, the ablation rate is determined by the optical penetration depth δ_{opt} (see Equation (1)). In contrast, the electron thermal diffusion length δ_{diff} dominates the transfer of laser energy into the target substrate at high laser fluences, according to Equation (2).

$$h = \delta_{opt} \bullet ln\left(\frac{F}{F_{th}}\right) \qquad \delta_{opt} \gg \delta_{diff} \qquad (1)$$

$$h = \delta_{diff} \bullet ln\left(\frac{F}{F_{th}}\right) \qquad \delta_{opt} \ll \delta_{diff} \qquad (2)$$

Experimentally it was also observed that the energy penetration depth depends strongly on the pulse duration, so that heat conduction effects are of great importance when ablating the target with ns-pulses.[76] Therefore, it is useful to generalize the logarithmic relation by introducing an effective penetration depth δ_{eff}, according to Equation (3).

$$h = \delta_{eff} \bullet ln\left(\frac{F}{F_{th}}\right) \qquad (3)$$

Fitting Equation (3) to the experimental data points in Figure 3 c allows calculating δ_{eff} by the slope of the linear fits (the fits are shown in the appendix in Figure S3). Furthermore, the ablation threshold fluence F_{th} can be derived from the intersection of the linear fit with the x-axis. Note that linear regression was performed for incident laser fluences of up to 166 J cm^{-2}, while higher laser fluences were neglected due to saturation of the ablation depth. The results of the calculation of the effective penetration depth and the ablation threshold fluence are summarized in Table 1. The experimental results are supplemented by the theoretical values of

Table 1. Optical penetration depth (δ_{opt}), thermal diffusion length (L_{th}), effective penetration depth (δ_{eff}), and ablation (F_{th}) and damage fluence threshold (F_d) as a function of the target material. $F_{th,theor}$ and $F_{d,theor}$ were calculated theoretically according to Equations (5) and (7).

	δ_{opt} [µm]	L_{th} [µm]	$\delta_{eff,exp}$ [µm]	$F_{th,theor}$ [J cm^{-2}]	$F_{th,exp}$ [J cm^{-2}]	$F_{d,theor}$ [J cm^{-2}]
Au	0.011	1.52	1.52 ± 0.06	3.31	2.31 ± 0.13	0.39
Ag	0.011	1.77	3.44 ± 0.26	2.93	1.46 ± 0.08	0.41
Cu	0.012	1.45	1.84 ± 0.13	2.62	2.44 ± 0.19	0.53
Fe	0.021	0.64	0.33 ± 0.08	1.23	0.36 ± 0.71	0.34
Ti	0.021	0.41	0.27 ± 0.08	1.35	0.01 ± 2.04	0.16
Al	0.009	1.33	5.35 ± 0.39	2.58	1.91 ± 0.18	0.21

the optical penetration depth (δ_{opt}), the thermal diffusion length (L_{th}), as well as the ablation ($F_{th,theor}$) and damage ($F_{d,theor}$) threshold fluence, which are discussed in detail below.

The material-related trend of the effective penetration depth is in line with the order of the ablation depth determined for SP-ns-LAL of the different target materials (see Figure 3 c). The effective penetration depth is several orders of magnitudes larger than the optical penetration depth, which was calculated considering the material-dependent absorption coefficients at 1064 nm (see Table 1 in the appendix). This large difference is expected for ns-LAL since, compared to ultrashort laser pulses, the pulse duration for ns-laser pulses is significantly longer than the characteristic electron-phonon-relaxation times. Hence, a local thermal equilibrium between the electronic and the lattice system can be assumed. In this case, Lambert–Beer's law no longer applies since the thermal diffusion length significantly exceeds the optical penetration depth, and heat conduction is no longer negligible. For a more detailed evaluation, the thermal diffusion lengths were calculated according to Equation (4).[80]

$$L_{th} = \sqrt{\frac{2\kappa\tau}{c_{p,s}}} \qquad (4)$$

Here, κ represents the thermal conductivity, τ the laser pulse duration, and $c_{p,s}$ the specific heat capacity of the ablated material (values are listed in Table S2 in the Supporting Information). For Au, the calculated thermal diffusion length and the effective penetration depth agree very well. Also, for Cu, Fe, and Ti, the values match well within one order of magnitude. However, larger deviations become visible for Ag and especially for Al. In the latter case, the effective penetration depth is four times higher than the thermal diffusion length, indicating that other effects contribute to the energy transfer into the target system. Likely exothermic redox reactions between the target material and water lead to additional energy release, further affecting the ablation process on a timescale later than the laser-matter interaction regime, as discussed later in more detail.

Regarding the experimentally determined ablation threshold fluences, comparable values around 1–2 J cm^{-2} were found for Au, Ag, Cu, and Al (see Table 1). For Fe and Ti, the ablation threshold fluences are significantly reduced. However, note that the R-squared values (see Figure S3) indicate an inaccuracy of the linear regression for these metals. Hence, the errors are several times larger than the calculated ablation thresholds, so that the results for Fe and Ti have to be handled with caution.

From a theoretical point of view, the ablation threshold fluence is controlled by the target materials' optical and physicochemical

Chemistry–A European Journal

Full Paper
doi.org/10.1002/chem.202005087

Chemistry Europe
European Chemical
Societies Publishing

properties. For ns-ablation, the ablation threshold can be estimated according to Equation (5), considering the energy ΔU required to heat, melt, and vaporize the target material, the thermal diffusion length L_{th} and the reflectivity R of the target materials.[81]

$$F_{th} = \frac{\Delta U}{L_{th} \bullet (1 - R)} \quad (5)$$

While the target materials' reflectivity was measured experimentally (see Figure S4 in the appendix), ΔU can be approximated by multiplying the heat of melting and vaporization by the material density (the material parameters are listed in Table S2). The magnitude of the theoretical threshold fluences agrees well with the experimental value except for Fe and Ti (see Table 1), further supported by the literature. For example, for ns-LAL of Au in water, an ablation fluence threshold of 3.7 J cm^{-2} was calculated.[82]

For the discussion of the different material-dependent trends related to the ablation depth and the spot diameter during SP-ns-LAL, the interaction of the laser pulse with the target material and the liquid (as well as secondary, post-laser-pulse target ablation) must be taken into account. Since materials with different melting and vaporization temperatures were studied, the resulting surface morphologies differ significantly.

Figure 4 shows exemplary SEM images of the ablation spots produced by SP-ns-LAL of Au, Ag, Cu, Fe, Ti, and Al in water at a laser fluence of 166 J cm^{-2}. At this point, it has to be emphasized that the surface roughness of the pristine bulk targets is not the same for all target materials, affecting their reflectivity and, consequently, the fluence ablation threshold.[83] For example, the surface roughness of the pristine Au or Ag bulk surface appears to be higher than that of the pristine Cu or Fe targets when looking at the SEM images, which is confirmed by the reflectivity of the corresponding bulk materials (see Figure S4). Therefore, it is expected that the ablation efficiency is slightly reduced for those materials (Cu, Fe) that are characterized by a higher reflectivity (about 20% higher for Cu and Fe compared to Au, Ag, Ti, and Al). However, recent studies have shown that the bulk material's reflectivity is of minor importance when the target is ablated with laser fluences far above the ablation threshold.[72,84] Since the incident laser fluence of 166 J cm^{-2} used for ablation is two orders of magnitude higher than the ablation threshold (see Table 1), it is concluded that differences in surface roughness can be neglected for the discussion of the SEM images. Nevertheless, the surface roughness is important
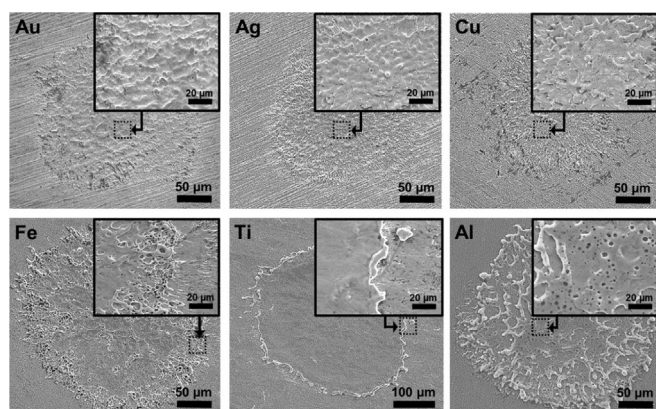
concerning incubation effects at lower incident laser fluences, discussed in more detail in the cavitation bubble section of this work.

When comparing the ablation craters formed on the different bulk materials, large differences in the resulting surface morphology become apparent. In the case of Au, Ag, and Cu, wavy structures on the ablated metal surface indicate that the melting of the target surface is accompanied by some kind of hydrodynamic instability.[52,53] Molten structures are also visible on the ablated Al surface. These are more dominant than on the other metals' surfaces and were pushed away from the center to the periphery of the ablation spot before solidification. This "pushing effect" is even more pronounced on the ablated Fe and Ti surfaces, resulting in melting edges (also visible on the confocal 3D images in Figure 3b) that are predominantly localized at the periphery of the ablation crater. While the high melting tendency for SP-ns-LAL of Al can partly be explained by its low melting point (933 K),[85] the formation of the melting edges on the ablated Ti and Fe surfaces is probably attributed to the low thermal diffusivity of these metals. The impact of the recoil pressure induced by the cavitation bubble likely further intensifies this effect.[75,86]

Another interesting feature becomes visible when one takes a closer look at the melt's topography (see inserts in Figure 4). The formation of a porous structure with different degrees of microcavities can be observed. The number of these micro-cavities is quite low for Au, Ag, and Cu but increases significantly for Fe and Al. In contrast, no micro-cavities are visible on the ablated Ti surface. It is often reported that the micro-cavities originate from phase explosion (besides spallation) of the target material.[76,87,88] It is further speculated that homogeneous bubble nucleation occurs when the melt's temperature rises to a value of 0.8–0.9 of the metal's critical thermodynamic temperature T_c. In this case, the hot molten layer is penetrated by the supercritical water, and hydrodynamic disintegration of this layer into NPs takes place.[53] Afterward, the liquid layer is pushed back to the target surface. Different values were reported for the critical thermodynamic temperature of the metals used in this study. For example, a T_c of 7400 K was found for Au,[89] while it is 6700 K for Al.[90] For Ti, the T_c of 11790 K[91] is far higher compared to the other metals, consistent with the lowest degree of micro-cavities.

Note that for water, the critical thermodynamic temperature is 647 K.[85] According to Starinskiy et al., the damage threshold for melting is balanced by the phase change temperature of water and the metal melting temperature.[82,92] For the ablation of metals with high melting points, water phase change starts before target melting, and for the ablation of metals with low melting points, it is the opposite. Therefore, it is expected that the damage threshold is higher for the ablation of high melting metals since the formed vapor-liquid interface shields the incoming laser beam.[82,92] The ablation depths were plotted against the different materials' melting temperatures for evaluating this relationship (Figure 5a). A good correlation between the ablation depths and the melting temperatures of the corresponding materials can be observed.

In the following, the material-specific trend of the measured spot diameters is discussed in more detail. Since the measured and theoretically calculated spot diameters differ (see Figure 1), the incident and effective laser fluence also differ, as demonstrated in Figure 5b. The incident laser fluence is calculated by dividing the applied pulse energy by the target area illuminated by the laser beam. Considering a pulse energy of 11.9 mJ and the theoretical spot sizes (which are material-independent), the incident laser fluences range from 21 to 313 J cm^{-2}. In contrast, the effective laser fluences were calculated by considering the effective spot size after ablation. Since the largest spot sizes were obtained for Ti, the
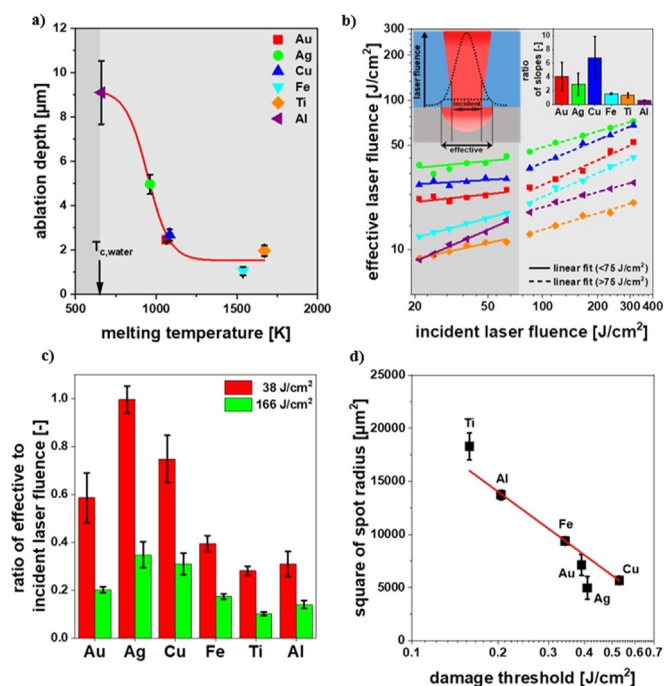

Figure 4. SEM images of ablation spots produced by SP-ns-LAL of Au, Ag, Cu, Fe, Ti, and Al in water at a theoretical, incident laser fluence of 166 J cm^{-2}. The insets show the surface morphology at higher magnifications.

Chemistry–A European Journal

Full Paper
doi.org/10.1002/chem.202005087

Chemistry Europe
European Chemical
Societies Publishing

Figure 5. (a) Ablation depth as a function of the bulk materials' melting points. The critical thermodynamic temperature of water is marked with an arrow. (b) Double logarithmic plot of the measured, effective laser fluence against the theoretical, incident laser fluence. Linear regression of the data obtained for theoretical, incident laser fluences below (solid lines) and above (dashed lines) 75 J cm^{-2} are included. In the insert, the ratio of the slopes >75 J cm^{-2} to <75 J cm^{-2} is plotted. (c) Ratio of the measured, effective to theoretical, incident laser fluence. The ratios were calculated for a fixed theoretical, incident laser fluence of 38 and 166 J cm^{-2}. (d) The squared effective spot radius obtained at a theoretical, incident laser fluence of 166 J cm^{-2} is shown as a function of the logarithmic calculated material-specific damage thresholds. A linear fit is used.

effective laser fluences are the smallest for this metal (11 ± 1 to 26 ± 3 J cm^{-2}). In contrast, the smallest spot sizes were measured for Ag so that the effective laser fluences are the highest for this metal (41 ± 4 to 92 ± 22 J cm^{-2}). The effective laser fluences of the other metals lie between those of Ag and Ti, following the order Ti < Al < Fe < Au < Cu < Ag.

It is worth mentioning that the deviation between the incident and effective laser fluence is smaller below an incident laser fluence of 75 J cm^{-2} but increases above this value. This trend is particularly pronounced for Au, Ag, and Cu, as indicated by the ratio of the slope of the linear fits between these two fluence regimes in the insert of Figure 5 b. This observation is further confirmed by the ratio between the effective and the incident laser fluence calculated for a fixed incident laser fluence of 38 and 166 J cm^{-2} in Figure 5 c. At an incident laser fluence of 38 J cm^{-2}, the ratio is 1.00 ± 0.06 for Ag and decreases from Cu (0.75 ± 0.09), Au (0.6 ± 0.1), Fe (0.39 ± 0.03), Ti (0.28 ± 0.02) to Al (0.31 ± 0.05). At a fixed incident laser fluence of 166 J cm^{-2}, the ratio of the effective to incident laser fluence is 2–3 times lower. This trend can be associated with a less efficient coupling of laser energy into the target system. At higher laser fluences, plasma shielding effects become more relevant.

Nevertheless, it remains unclear how the effective spot diameters relate to the target materials' physicochemical properties. For a first assessment, the spatial fluence distribution F(x) is considered,

which is given by Equation (6), assuming a Gaussian beam (the M^2 value of the used laser is 2 and delivers TEM$_{00}$ mode).

$$F(x) = F_0 \bullet \exp\left(\frac{-x^2}{w_o^2}\right) \tag{6}$$

Here, x represents the distance from the beam center, F_0 the peak fluence at the beam center, while ω_0 is defined as the $1/e^2$ beam radius of the distribution. The laser fluence is the highest in the beam center but decreases exponentially with increasing distance, as outlined in the insert of Figure 5 b. The fluence falls below the ablation threshold at a certain distance from the beam center, where the impact of target annealing, modification, and melting increases. Taking into account the thermal diffusion length L_{th} (from Table 1), the melting temperature T_m, the specific heat capacity $c_{p,s}$ as well as the density ρ of the different bulk materials (from Table S2 in the appendix) and the ambient temperature T_0 (298 K), the material-specific damage threshold $F_{d,m}$ for melting can be calculated by Equation (7).[80]

$$F_{d,m} = c_{p,s} \bullet \rho \bullet (T_m - T_0) \bullet L_{th} \tag{7}$$

In Figure 5 d, the calculated damage thresholds (also summarized in Table 1) were plotted against the squared effective spot radius at an exemplary incident laser fluence of 166 J cm^{-2}. The values correlate very well, indicating that the effective spot size (and thus the effective laser fluence) is determined by the SP-ns-LAL-induced melting of the target surface depending on the ablated materials' thermal properties.

Characterization of the cavitation bubble dynamics

As predicted by MD simulations, the hot molten layer that forms in the initial phase after laser-matter interaction strongly interacts with the liquid, resulting in an expanding low-density metal-water mixing region, which serves as the precursor for the formation of the cavitation bubble.[53,54] Although this mixing region offers suitable conditions for chemical reactions, these have not yet been considered in the MD simulations. Such chemical reactions include redox reactions that can take place between the molten material and supercritical water, further affecting the evolution of the cavitation bubble. Therefore, the influence of the redox potential of the target materials on the cavitation bubble evolution is investigated in the following. Generally, the lifetime and the size of the cavitation bubble strongly depend on the applied pulse energy[45–47] and the focusing conditions.[47] However, for the first bubble expansion phase, it was found that the bubble maximum is always located at the same time delay of 80 μs regardless of the applied laser fluence and target material (see Figure S5a). Therefore, a constant time delay of 80 μs was chosen for all further experiments. Figure 6a shows pictures of the maximum cavitation bubble volumes recorded during SP-ns-LAL of Au, Ag, Cu, Fe, Ti, and Al.

The cavitation bubbles produced on the different materials exhibit a quasi-hemispherical shape at their maximum expansion with a sharp interface to the liquid phase. The cavitation bubbles' sizes are comparable for Au, Ag, Cu, Fe, and Ti and are characterized by heights and diameters of 1.6 mm and 3.2 mm, respectively. However, for Al, the cavitation bubble is much bigger, reflected in an enlargement in bubble height and diameter by 200 μm (indicated by red-dashed, horizontal line). The bubble volume was calculated, considering the cavitation bubble height and diameter (Figure 6b). Analogous to the ablation depth (compare Figure 3c), the bubble
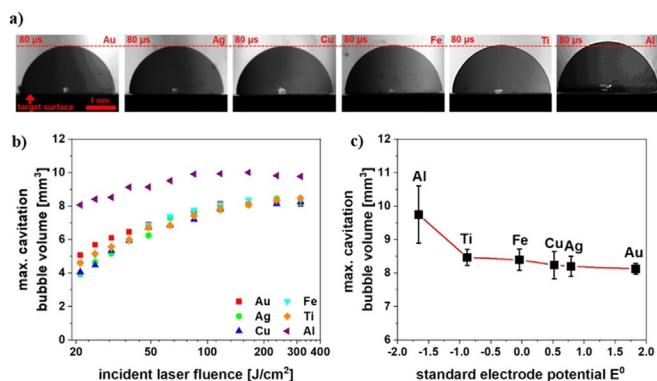
Chemistry–A European Journal

Full Paper
doi.org/10.1002/chem.202005087

Chemistry
Europe
European Chemical
Societies Publishing

Figure 6. (a) Pictures of cavitation bubbles produced during SP-ns-LAL of Au, Ag, Cu, Fe, Ti, and Al in water at a theoretical, incident laser fluence of 313 J cm^{-2}. Each picture was recorded at a constant time delay of 80 µs after the laser impact, representing the maximal expansion phase. (b) Maximum cavitation bubble volume depending on the target material and the theoretical, incident laser fluence. (c) Maximum cavitation bubble volume as a function of the standard electrode potential of the ablated material.

volume increases with increasing incident laser fluence but saturates and approaches constant values of about 8 mm^3 at laser fluences above 166 J cm^{-2}.

Interestingly, there is no clear trend in bubble volume for incident laser fluences below 63 J cm^{-2} for all materials except Al. In this low-fluence regime, the bubble volumes are smallest for Ag and Cu, followed by Ti, Fe, and Au. This trend is probably due to the impact of incubation effects.[81] Reich et al. reported that such incubation effects are more important in the low-fluence regime, where the cavitation bubble size increases significantly during the first few laser pulses. They explained the findings by a suppressed target reflectivity and more efficient coupling of laser energy into the target.[72] In the high-fluence regime, incubation effects are of minor importance. Hence, the target reflectivity or roughness of the pristine target surface seems to be less-relevant in the high-fluence regime where the cavitation bubble volumes are comparable for all materials except Al. This observation is further supported by Bevanides et al., who showed that the reflectivity drops significantly during ns-ablation when the laser fluence is much higher than the ablation threshold.[84]

In contrast to the other materials, the bubble volumes are consistently the largest for Al regardless of the incident laser fluence. In the low-fluence regime, the maximum bubble volume is almost twice as large compared to the other metals. With increasing incident laser fluence, the differences decrease, but the LAL-induced cavitation bubble on Al is still 20 % bigger. Recently, it was shown that the hydrogen gas formation rate increases strongly with increasing oxidation sensitivity of the ablated material.[62,63] Possibly, not only the formation of persistent bubbles is influenced by the oxidation-sensitivity of the ablated material, but also the formation of the initial cavitation bubble explaining the larger bubble volumes for Al. In this context, Tamura et al. found that a thin vapor layer (stated as the birth of the cavitation bubble) forms around the plasma boundary already during the first few tens of nanoseconds after laser-matter interaction, indicating a strong interaction of the plasma with the liquid.[93] Lam et al. showed that during ns-LAL of Al$_2$O$_3$ in water, Al atoms are oxidized after 2 µs.[21] Thus, the possibility of early redox reactions between the target material and water molecules would be given.

For further evaluation, the maximum cavitation bubble volumes were plotted as a function of the target materials' standard elec-

trode potential in Figure 6c. In contrast to the strong dependence of the total gas volume produced by ns-LAL from the target's redox potential[62,63] under SP-conditions, the redox potential dependence of the cavitation bubble volume is less prominent. For Au, Ag, Cu, Fe, and Ti, the cavitation bubble volume increases only slightly but steadily with decreasing standard electrode potential. However, considering the standard deviation, it is concluded that the cavitation bubble volume is less affected by the oxidation sensitivity of these metals under SP-ns-LAL conditions. The highest cavitation bubble volume of 9.8±0.8 mm^3 for Al, on the other hand, qualitatively agrees with the expectations of the redox chemistry. However, concerning the far higher molar ablation yield for Al (factor 12, see Figure 8a as will be discussed later) as well as factor 20 higher mole-specific gas formation volume compared to Au,[62,63] this cavitation bubble volume is still far smaller as expected, indicating that secondary effects contribute to both target ablation and gas formation rate at longer timescales.

Since the biggest difference in the cavitation bubble evolution was observed for Al, this material is discussed in more detail using Au as oxidation-inert reference material. For this purpose, the whole cavitation bubble cycle was recorded for both metals, as illustrated in Figure 7a. The development of the cavitation bubble can be subdivided into four stages.[45,46] In the first stage, the liquid undergoes phase transition inducing the formation of an expanding cavitation bubble. After reaching a stationary point with maximum size, the cavitation bubble begins to shrink and finally collapses. If enough energy is stored within the first cavitation bubble, one or more cavitation bubble rebounds are observed (second and third stage). Finally, all collapses and, in particular, the final collapse led to the formation of persistent bubbles (fourth stage).

By comparing the cavitation bubble's temporal evolution, it becomes apparent that the maximum cavitation bubble volume for Al is significantly larger than for Au, as discussed before. This observation applies not only to the maximum cavitation bubble volume but also to the entire first bubble cycle. Besides, the lifetime of the first cavitation bubble is longer for Al ($\approx$200 µs) than for Au ($\approx$180 µs), which is indicated by the red (for Au) and purple (for Al) colored vertical lines in Figure 7b, and further supported by the calculated Rayleigh collapse times (see Table S3 in the Supporting Information).

In the second stage (=first rebound), a secondary cavitation bubble is formed, which lasts longer and is larger for Al (350 µs and 1.6 mm^3) than for Au (330 µs and 1.2 mm^3), as expected from the bigger first bubble. However, a larger difference becomes apparent when looking at the third stage, which cannot be explained by Rayleigh–Plesset- or Gilmore-like bubble rebound behavior[94] and indicates strongly non-adiabatic conditions. For Au, only a small third cavitation bubble (2nd rebound) is formed, collapsing after 390 µs and characterized by a maximal bubble volume of 0.3 mm^3. The cavitation bubble formed on the Al surface is three times larger (1.1 mm^3) and lasts significantly longer (510 µs), indicating that another process contributes to the bubble rebound extent.

In this context, the ratio of the individual cavitation bubble lifetimes T_{osc} is interesting as it represents an expression of the vigor of the bubble collapse. The ratio increases with increasing collapse pressure and damping induced by the acoustic transient or shockwave emission. The T_{osc1}/T_{osc2} ratio is larger for Al (1.45) than for Au (1.22). It is known from SAXS measurements that the LAL-induced cavitation bubbles contain ablated matter.[48–50,58] Additionally, water is decomposed during LAL, and a large quantity of permanent gases is formed depending on the oxidation-sensitivity of the ablated material.[62,63] Thus, it is likely that the cavitation bubble
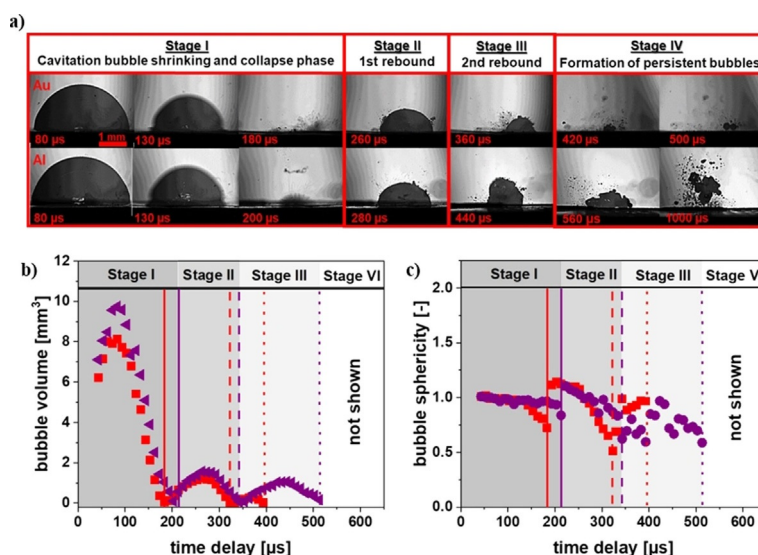
Chemistry–A European Journal

Full Paper
doi.org/10.1002/chem.202005087

Chemistry Europe
European Chemical
Societies Publishing

Figure 7. (a) Temporal evolution of the cavitation bubble on gold (upper picture series) and aluminum target (lower picture series) immersed in water at a theoretical, incident laser fluence of 313 J cm^{-2}. (b) Temporal evolution of the cavitation bubble volume and (c) calculation of the bubble sphericity (hemi-spherical = 1.0) as a function of time. Au = red squares, Al = purple circles.

also consists of permanent gases besides ablated matter and water vapor. More non-condensable bubble content then leads to a stronger cushioning of the collapse and less damping by shock-wave emission. Also, the Rayleigh–Plesset and Gilmore equations cannot account for symmetry breaking at the bubbles' interface layer which extent depends on the liquid viscosity[94] and is expected to have a stronger effect for smaller (rebounding) bubbles.

After the final bubble collapse, persistent bubbles (indicated as dotted red and purple lines) are formed. The amount of these bubbles is significantly larger for Al than for Au, which can be explained by the high redox affinity of Al to water.[62, 63] Considering that such redox reactions are exothermic, they likely contribute to the energy transfer into the bubble rebound and/or additional formation of (permanent) gas, leading to a larger bubble rebound volume and lifetime.

The picture frames further indicate that the cavitation bubbles deviate from the ideal hemispherical shape. This deviation is particularly pronounced during the second rebound event on the Al surface. The bubble sphericity was calculated to evaluate this symmetry deviation in more detail (Figure 7c). It is defined by the ratio of bubble height (expansion in the y-direction) to bubble radius (expansion in the x-direction) considering a hemispherical bubble geometry according to Equation (8).

$$bubble\ sphericity = \frac{bubble_{height}}{bubble_{radius}} \tag{8}$$

Accordingly, a symmetry factor of 1 is associated with an ideal hemisphere. The bubble sphericity is ideal for both materials during the maximum expansion phase but decreases as the first rebound event approaches. The decrease of the bubble sphericity is larger for Au than for Al. However, its value increases again at the beginning of the first rebound stage, followed by a steady decrease until the second rebound is reached. During the third stage, the bubble sphericities for Au and Al are completely different. In the case of Au, the bubble sphericity increases until an almost hemispherical bubble is reached, whereas the bubble sphericity fluctuates for Al (visible as bumpy structures in Figure 7a). This change in sphericity is probably due to the strong reactivity of Al

with the water (vapor) phase and the stronger cushioning of the bubble induced by the formation of less-condensable permanent gases.

Correlation of the amount of ablated matter with the cavitation bubble properties

Since the ablated matter and its reactivity with water seem important for the cavitation bubble dynamics, the volumetric, mass, and molar ablation efficiencies were determined by confocal 3D microscopy. The results are summarized as stacked bar charts in Figure 8 a–c (the data points for each metal are given in Figure S6 in the Supporting Information).

The volumetric ablation efficiency is the highest for Al. It increases almost linearly from $1.7 \pm 0.7 \times 10^5$ to $3.5 \pm 0.5 \times 10^5$ µm³/pulse until an incident laser fluence of 166 J cm^{-2} is reached. A further increase of the incident laser fluence is accompanied by saturation of the volumetric ablation efficiency. For Au ($0.2 \pm 0.1 \times 10^5$ to $0.3 \pm 0.1 \times 10^5$ µm³/pulse), Ag ($0.14 \pm 0.1 \times 10^5$ to $0.8 \pm 0.1 \times 10^5$ µm³/pulse), and Cu ($0.1 \pm 0.0 \times 10^5$ to $0.4 \pm 0.1 \times 10^5$ µm³/pulse), the volumetric ablation efficiency shows the same dependence on the incident laser fluence but is in total up to ten times lower than for Al. In contrast, the general trend for Fe ($0.3 \pm 0.0 \times 10^5$ to $0.1 \pm 0.0 \times 10^5$ µm³/pulse) and Ti ($0.8 \pm 0.1 \times 10^5$ to $0.4 \pm 0.1 \times 10^5$ µm³/pulse) is the opposite. The ablated volumes are highest at low incident laser fluences and decrease steadily with increasing incident laser fluence. This trend can be attributed to the formation of melting edges (see Figure S2), which do not contribute to the ablated volume.

For further evaluation, the volumetric ablation efficiencies were divided by the material density to obtain the mass ablation efficiency (Figure 8b). A mass ablation efficiency range from 0.1 to 1 µg/pulse is equivalent to a range from 10 to 100 mg/(hW) assuming, e.g., a 1 kHz, 30 mJ continuous ns-LAL process. According to Figure 8b, the efficiency in SP-ns-LAL is around a factor of 10 higher than observed for kHz-systems[62, 63] indicating the significant loss of efficiency due to shielding effects. In detail, SP-ns-LAL ablation efficiencies are highest for Ag and Al (≈ 1 µg/pulse) and decrease to 0.1–0.5 µg/pulse for Au, Cu, Fe, and Ti. Thus, the mass ablation

Chemistry–A European Journal

Full Paper
doi.org/10.1002/chem.202005087

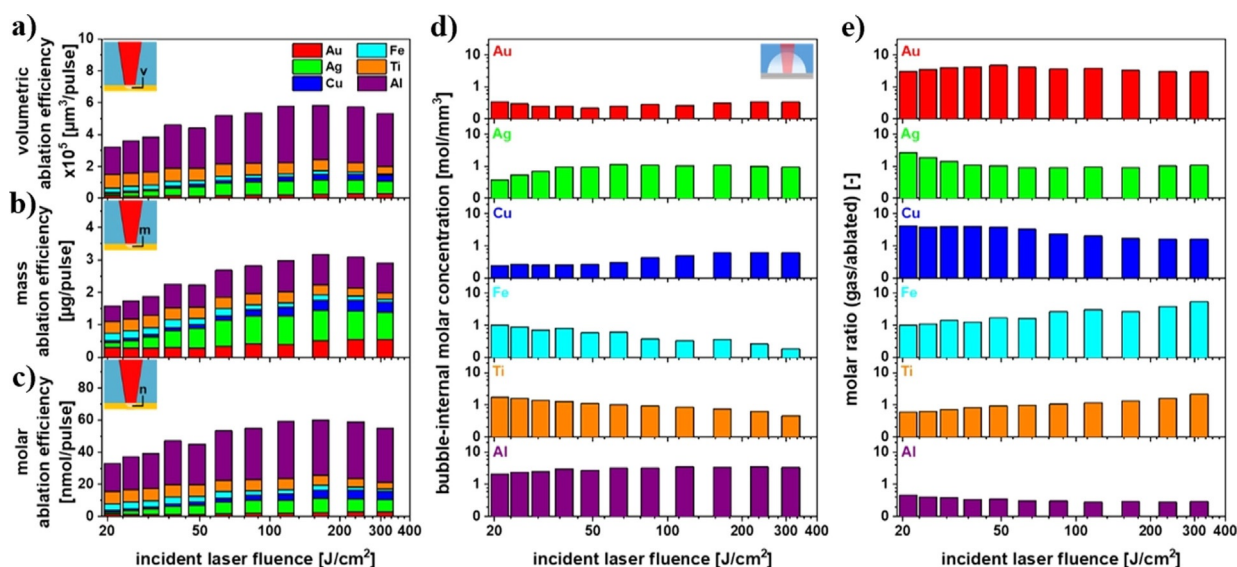**Chemistry
Europe**
European Chemical
Societies Publishing

Figure 8. (a–c) Stacked chart summarizing the volumetric, mass, molar ablation efficiency measured by confocal 3D microscopy for SP-ns-LAL of Au, Ag, Cu, Fe, Ti, and Al in water. (d) Virtual (i.e., not experimentally determined but calculated) bubble-internal molar concentration and (e) ratio of the molar gas amounts contained in the cavitation bubble to the amount of ablated mol depending on the theoretical, incident laser fluence.

efficiency does not correlate with the redox potential of the ablated material under SP-ns-LAL conditions, as was observed for continuous ns-LAL of the same metals with repetition rates in the kHz range.[62,63] The different trends can be explained by the fact that the formation of persistent bubbles starts after several hundred microseconds (see Figure 7). Hence, their influence on the first laser pulse is negligible so that the ablation yield in SP-LAL is not affected by gas formation cross-effects. However, it has been shown that the redox chemistry between the ablated matter and the water phase might be important for cavitation bubble dynamics. Since such redox reactions are typically balanced by the reaction stoichiometry of the involved redox pair (metal and water), the molar ablation efficiency was calculated by dividing the mass ablation efficiency by the corresponding material's molar mass (see Figure 8c). The molar ablation efficiencies are the highest for Al (35 nmol/pulse) and decrease to 2–8 nmol/pulse for Ag, Ti, Cu, Fe, and Au. Surprisingly, SP-LAL of Ag leads to a significantly higher ablation efficiency than for SP-LAL of Au. On the one hand, Ag has half the density of Au. On the other hand, Ag has a bigger thermal diffusion length leading to deeper craters. Possibly, Ag is a material that presents a good balance between heat penetration and heat dissipation. Also, the difference in surface morphology may have caused the high energy in-coupling.[95] It is clear that more detailed studies are needed on this topic. Methods such as ps-resolved pump-probe microscopy[96] or ellipsometry[97] could help to understand the different target material behavior.

In the next step, the molar ablation efficiency was related to the cavitation bubble volume, resulting in the bubble-internal molar concentration (Figure 8d). Note that the presented concentration values are the nominal bubble-internal concentrations assuming that the target mass derived from the crater volume measurements is present in total in the first bubble. This ideal situation is not the case in particular for redox-active targets, as will be discussed later, and calculation of this ideal value intends to demonstrate the deviance from this "ideal" (redox-reaction-free) behavior. For Au, this virtual bubble-internal molar concentration is about 0.3 nmol/mm^3 and remains rather constant over the entire fluence range. For Ag, Cu, and Al, it increases with increasing laser fluence,

resulting in maximum concentrations of 1 nmol/mm^3, 0.6 nmol/mm^3, and 3.5 nmol/mm^3, respectively. For Fe and Ti, the trend is the opposite, so that the bubble-internal molar concentrations of 1–2 nmol/mm^3 are the highest in the low-fluence regime. Overall, the nominal concentration of ablated matter (if the laser pulse causes the whole crater volume) of Al would be a factor of ten higher than for Au.

Letzel et al. determined a bubble-internal molar concentration of 3.7 nmol/mm^3 for SP-ns-LAL of Ag in water at an effective laser fluence of 14.5 J cm^{-2}.[73] In the present study, a ten times lower concentration of 0.4 nmol/mm^3 was determined at a comparable incident laser fluence of 21 J cm^{-2}, unexpected at first sight. However, note that Letzel et al. ablated the target with ten single pulses or more to obtain accurate ablation results and extrapolated these values to one pulse. Hence, incubation effects may be responsible for the differences in the bubble-internal molar concentrations.

For further discussion, the molar gas amount in the cavitation bubble was calculated for Au and Al as reference materials to assess the influence of redox reactions within the bubble cavity. Assuming that the total amount of ablated mol Al (35 nmol at an incident laser fluence of 313 J cm^{-2}) reacts with water, ca. 50 nmol molecular hydrogen is expected to be formed. A comparison of this value with the gas volume of 1.6 mm^3 obtained by subtracting the experimentally found cavitation bubble volume for Al (9.8 mm^3) from that of Au (8.2 mm^3) would support the theory of early redox reactions. However, two points are disregarded. Firstly, the redox potential is temperature-dependent, so that already simple calculation of the temperature-dependent Nernst equation predicts oxidation of gold (i.e. if the overpotential is taken into account).[35] Secondly, the assumption that the total mass is ablated within the laser pulse and plume time regime is probably incorrect, particularly for (exothermic) redox-active target materials. The latter point is further supported by considering the molar ratio of the amount of gas in the first cavitation bubble to the amount of ablated matter (Figure 8e). This molar ratio would predict that the contribution of Au to the gas volume of the primary cavitation bubble is ten times higher than that of Al, which is unrealistic from the viewpoint of the redox chemistry and the assumption that the

Chemistry–A European Journal

Full Paper
doi.org/10.1002/chem.202005087

Chemistry Europe
European Chemical
Societies Publishing

ablated mass (from Figure 8a) is completely present in the first bubble. Therefore, exothermic reactions at the target surface likely contribute to the ablation of additional material, which further affects the second rebound of the cavitation bubble and the formation of persistent bubbles (compare Figure 7). This assumption is supported by Reich et al., who have shown that the oxidation of Zn atoms present in the liquid sets in at time delay after the collapse of the first cavitation bubble.[98]

For a more detailed discussion, the exothermic character of the redox reaction of the metals with water was investigated. This reaction can induce the release of additional heat, which amount can be approximated by taking into account the corresponding reaction enthalpy[85,99] and the molar amount of ablated matter, as demonstrated in Table 2.

For less-oxidation-sensitive metals such as Au, Ag, Cu, and Fe, the redox reaction with water is endothermic but becomes exothermic for Ti and Al. Related to the initial pulse energy of 11.9 mJ, this

means that the exothermic redox reaction of Ti and Al with water generates 17 and 240% additional energy, respectively. These strong non-adiabatic exothermic conditions probably influence not only the ablation yield on a timescale later than the laser pulse and plume time regime but also the cavitation bubble rebound and the formation of persistent bubbles.

Mechanistic picture summarizing the physical and chemical processes during LAL

The mechanistic picture displayed in Figure 9 summarizes the chemical and physical processes that possibly occur within the different temporal stages during ablation in water and determine the ablation yield, the vaporization and decomposition of the liquid, the cavitation bubble dynamics, and the formation of persistent bubbles and NPs.

Based on the laser pulse interaction with the target material (Figure 9, panel 1), the pulse duration is important because it determines the rate and depth of the deposition of laser energy into the target material.[76,100] While for ultrashort pulses (fs-ps), the deposition of laser energy takes place within the range of the optical penetration depth of the target material,[76] for longer laser pulses ($\geq$ ns), deeper parts of the target material are affected by heat conduction.[101,102] In a liquid environment, the effective energy penetration depth might be even higher than expected for ablation in air since exothermic reactions between oxidation-sensitive metals and water induce the release of additional energy from that confined volume that penetrates the target and affects the ablation yield, probably including the timescale later than the laser pulse and plume time regime.

The ablation process (Figure 9, panel 2) is driven by the strong interaction of the ablation plume with the liquid, which is rapidly
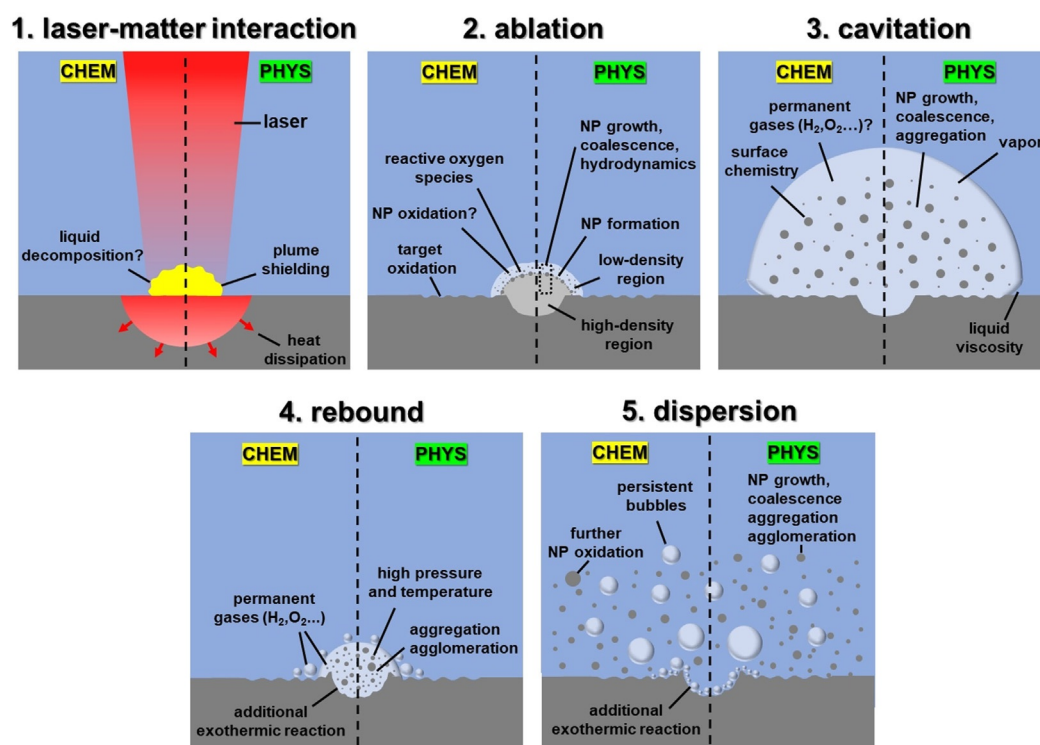
Table 2. Calculation of the amount of heat formed during the reaction of water and ablated matter based on the ablated mass at a theoretical, incident laser fluence of 313 J cm^{-2} and enthalpy values from literature.[85,99]

Material	Reaction enthalpy [kJ mol^{-1}]	Amount of ablated mol [nmol]	Energy [mJ]
Au	845	2.8 ± 0.2	2.39 ± 0.17
Ag	255	8.8 ± 1.6	2.24 ± 0.41
Cu	123	5.2 ± 0.2	0.64 ± 0.02
Fe	20	2.2 ± 1.4	0.04 ± 0.02
Ti	−372	5.5 ± 0.5	−2.04 ± 0.18
Al	−818	35.1 ± 9.1	−28.7 ± 7.44

Figure 9. Scheme of the physical and chemical processes occurring during laser-matter interaction (1), ablation (2), cavitation (3), and rebound (4) of the cavitation bubble as well as the dispersion (5) of persistent bubbles and NPs within the liquid.

Chemistry–A European Journal

Full Paper
doi.org/10.1002/chem.202005087

Chemistry Europe
European Chemical
Societies Publishing

heated to supercritical conditions resulting in the formation of an expanding low-density metal–water mixing region.[52,53] This region provides suitable conditions for the nucleation and growth of small NPs as well as chemical reactions.

Even though the oxidation of the target surface and NPs is a commonly observed phenomenon,[57,62,63,75,103] the time and place of oxidation are controversially discussed. Since reactive oxygen species are formed within the plasma,[62,63,104] it is not unlikely that the NPs are oxidized within the low-density metal-water mixing region, which further expands, leading to the evolution of the cavitation bubble (Figure 9, panel 3). The cavitation bubble, of which the contact angle with the target surface strongly depends on the liquid viscosity,[94] acts as confinement for the particle mass. Its interior consists mainly of solvent molecules.[55,105] However, permanent gases such as molecular hydrogen and oxygen formed by early plasma-liquid[44] or redox reactions within the low-density water-metal mixing region are also likely present, as indicated within this study.

The NPs contained in the cavitation bubble are subject to even further reactions.[57,58,98] Nevertheless, it is unclear to what extent the NPs in the cavitation bubble result from the ablated mass within the laser pulse and plume time regime since hints were found in this study that redox-active materials may react exothermally with water, resulting in an additional energy release, which probably leads to further material expulsion on a later timescale. Such strong, non-adiabatic conditions not only favor a larger second cavitation bubble rebound (Figure 9, panel 4), which cannot be explained by the Rayleigh-Plesset[55] and Gilmore-like rebound[106] behavior, for which adiabatic conditions (and symmetry) are assumed. Also, the formation of a large amount of persistent bubbles consisting of molecular hydrogen and oxygen near the target surface is promoted (Figure 9, panel 5), determining the NP productivity during continuous LAL.[60,62,63] After the final cavitation bubble collapse, the NPs are dispersed in the liquid, where they further grow[107] and oxidize[57,62,63,98] on the long-timescale.

In summary, all these physical and chemical processes discussed in this section demonstrate that the redox chemistry between the target material and the liquid is crucial for the ablation yield, cavitation bubble dynamics, and the formation of permanent gases on both the short- and the long-timescale. In particular, the exothermic character of these redox reactions in correlation with the physicochemical properties of the target materials (e.g., melting point and thermal diffusivity) is of high relevance for evaluating the LAL-induced ablation dynamics and should be further investigated in future studies.

Conclusions

The synthesis of colloids by laser ablation in liquids can be performed with a huge variety of different material classes. Since different physical and chemical properties characterize these materials, the outcome of the interplay between the laser, the bulk material, and the liquid is very complex. Laser ablation of oxidation-sensitive materials in water, e.g., promote the decomposition of water, further influencing the ablation process in terms of ablation efficiency, cavitation, and oxidation of the NPs. Such cross-effects are not only a nuisance for the upscaling of the process but also for fundamental investigations. Therefore, single-pulse ablation conditions are required to link the ablation yield to cavitation dynamics, disentangled from any post-irradiation effects.

By performing single-pulse nanosecond laser ablation of six different bulk materials (Au, Ag, Cu, Fe, Ti, and Al) in water, it was dem-

onstrated that the ablation characteristics are determined by the bulk material's thermal properties and redox potential. It was shown that the effective spot sizes vary significantly, resulting in spot sizes twice as large for poor thermal conductors like Fe and Ti, compared to good thermal conductors such as Au, Ag, and Cu. Consequently, the deviation from the effective and the incident laser fluence is largest for Ti and Fe with a factor of 5–8. For Au, Ag, and Cu, it was shown the deviations are smaller in the low fluence regime (factor 1–2) but increase significantly in the high fluence regime (factor 3–5) due to increasing importance of plasma shielding effects. Single-pulse ablation of low melting point, chemically reactive materials such as Al constitutes a border case that leads to large spot sizes, deepest crater structures, and thus highest ablation yields. These results are completely different from those observed for multiple pulsed laser ablation, where the formation of persistent bubbles determines the ablation efficiency on the long-timescale, making kHz-LAL of Al very ineffective.

Furthermore, in this study, we found indications that exothermic redox reactions between the target material and water are important for the cavitation bubble's volume and dynamics. It was shown that compared to oxidation-resistant target materials such as Au, 20% larger cavitation bubbles are formed on highly oxidation-sensitive materials such as Al. The difference in bubble volumes indicates that the cavitation bubble probably contains molecular hydrogen (and oxygen) in addition to water vapor. The formation of such non-condensable permanent gases combined with the exothermic redox reaction character influences the cavitation bubble dynamics, leading to a prolonged oscillation cycle and rebounds that are far larger than expected for adiabatic conditions. Therefore, target energy transfer (exothermic reaction) and permanent gas formation near the target surface need to be considered as key effects that contribute to both the reaction of the liquid with the target material and the ablation yield. As the chemical environment inside the cavitation bubble does affect the NP growth, determining its gas composition besides the nanomaterial's characterization could be interesting for future experiments.

Conflict of interest

The authors declare no conflict of interest.

[1] A. Karimi, J. Martin, *Int. Met. Rev.* **1986**, *31*, 1–26.
[2] C. Heathcock, B. Protheroe, A. Ball, *Wear* **1982**, *81*, 311–327.
[3] R. Richman, W. McNaughton, *Wear* **1990**, *140*, 63–82.
[4] A. Patist, D. Bates, *Innovative Food Sci. Emerging Technol.* **2008**, *9*, 147–154.
[5] D. Bermúdez-Aguirre, T. Mobbs, G. V. Barbosa-Cánovas, *Ultrasound applications in food processing*, Springer, Berlin, **2011**.
[6] C. Pétrier, A. Francony, *Ultrason. Sonochem.* **1997**, *4*, 295–300.

Chemistry–A European Journal | Full Paper
doi.org/10.1002/chem.202005087

Chemistry
Europe
European Chemical
Societies Publishing

[7] C. Petrier, A. Francony, *Water Sci. Technol.* **1997**, *35*, 175–180.

[8] K. S. Suslick, M. M. Mdleleni, J. T. Ries, *J. Am. Chem. Soc.* **1997**, *119*, 9303–9304.

[9] A. Vogel, W. Hentschel, J. Holzfuss, W. Lauterborn, *Ophthalmology* **1986**, *93*, 1259–1269.

[10] A. Vogel, M. Capon, M. N. Asiyo-Vogel, R. Birngruber, *Invest. Ophthalmol. Visual Sci.* **1994**, *35*, 3032–3044.

[11] A. Kruusing, *Opt. Lasers Eng.* **2004**, *41*, 329–352.

[12] D. Zhang, B. Gökce, S. Sommer, R. Streubel, S. Barcikowski, *Appl. Surf. Sci.* **2016**, *367*, 222–230.

[13] D. Zhang, B. Ranjan, T. Tanaka, K. Sugioka, *Int. J. Extreme Manuf.* **2020**, *2*, 015001.

[14] D. Zhang, B. Gökce, S. Barcikowski, *Chem. Rev.* **2017**, *117*, 3990–4103.

[15] S. Jendrzej, B. Gökce, M. Epple, S. Barcikowski, *ChemPhysChem* **2017**, *18*, 1012–1019.

[16] R. Streubel, S. Barcikowski, B. Gökce, *Opt. Lett.* **2016**, *41*, 1486–1489.

[17] R. Streubel, G. Bendt, B. Gökce, *Nanotechnology* **2016**, *27*, 205602.

[18] W. T. Nichols, T. Sasaki, N. Koshizaki, *J. Appl. Phys.* **2006**, *100*, 114911.

[19] F. Mafuné, J.-Y. Kohno, Y. Takeda, T. Kondow, H. Sawabe, *J. Phys. Chem. B* **2001**, *105*, 5114–5120.

[20] B. Gökce, D. D. van't Zand, A. Menéndez-Manjón, S. Barcikowski, *Chem. Phys. Lett.* **2015**, *626*, 96–101.

[21] J. Lam, D. Amans, F. Chaput, M. Diouf, G. Ledoux, N. Mary, K. Masenelli-Varlot, V. Motto-Ros, C. Dujardin, *Phys. Chem. Chem. Phys.* **2014**, *16*, 963–973.

[22] C. L. Sajti, R. Sattari, B. N. Chichkov, S. Barcikowski, *J. Phys. Chem. C* **2010**, *114*, 2421–2427.

[23] V. Amendola, D. Amans, Y. Ishikawa, N. Koshizaki, S. Scirè, G. Compagnini, S. Reichenberger, S. Barcikowski, *Chem. Eur. J.* **2020**, *26*, 9206–9242.

[24] C. Rehbock, J. Jakobi, L. Gamrad, S. Van der Meer, D. Tiedemann, U. Taylor, W. Kues, D. Rath, S. Barcikowski, *Beilstein J. Nanotechnol.* **2014**, *5*, 1523–1541.

[25] F. Waag, Y. Li, A. R. Ziefuß, E. Bertin, M. Kamp, V. Duppel, G. Marzun, L. Kienle, S. Barcikowski, B. Gökce, *RSC Adv.* **2019**, *9*, 18547–18558.

[26] O. Prymak, J. Jakobi, C. Rehbock, M. Epple, S. Barcikowski, *Mater. Chem. Phys.* **2018**, *207*, 442–450.

[27] M. S. S. Bharati, B. Chandu, S. V. Rao, *RSC Adv.* **2019**, *9*, 1517–1525.

[28] J. Zhang, D. N. Oko, S. B. Garbarino, R. G. Imbeault, M. Chaker, A. C. Tavares, D. Guay, D. Ma, *J. Phys. Chem. C* **2012**, *116*, 13413–13420.

[29] G. Compagnini, A. A. Scalisi, O. Puglisi, *J. Appl. Phys.* **2003**, *94*, 7874–7877.

[30] D. Werner, S. Hashimoto, T. Tomita, S. Matsuo, Y. Makita, *J. Phys. Chem. C* **2008**, *112*, 1321–1329.

[31] J. Jakobi, A. Menéndez-Manjón, V. S. K. Chakravadhanula, L. Kienle, P. Wagener, S. Barcikowski, *Nanotechnology* **2011**, *22*, 145601.

[32] S. Jendrzej, B. Gökce, S. Barcikowski, *Chem. Eng. Technol.* **2017**, *40*, 1569–1576.

[33] S. Petersen, S. Barcikowski, *J. Phys. Chem. C* **2009**, *113*, 19830–19835.

[34] C. Streich, L. Akkari, C. Decker, J. Bormann, C. Rehbock, A. Müller-Schiffmann, F. C. Niemeyer, L. Nagel-Steger, D. Willbold, B. Sacca, *ACS Nano* **2016**, *10*, 7582–7597.

[35] S. Reichenberger, G. Marzun, M. Muhler, S. Barcikowski, *ChemCatChem* **2019**, *11*, 4489–4518.

[36] S. Kohsakowski, R. Streubel, I. Radev, V. Peinecke, S. Barcikowski, G. Marzun, S. Reichenberger, *Appl. Surf. Sci.* **2019**, *467*, 486–492.

[37] D. Zhang, J. Liu, P. Li, Z. Tian, C. Liang, *ChemNanoMat* **2017**, *3*, 512–533.

[38] E. Bertin, A. Muenzer, S. Reichenberger, R. Streubel, T. Vinnay, H. Wiggers, C. Schulz, S. Barcikowski, G. Marzun, *Appl. Surf. Sci.* **2019**, *467*, 1181–1186.

[39] T. Hupfeld, T. Laumer, T. Stichel, T. Schuffenhauer, J. Heberle, M. Schmidt, S. Barcikowski, B. Gökce, *Procedia CIRP* **2018**, *74*, 244–248.

[40] M. B. Wilms, R. Streubel, F. Frömel, A. Weisheit, J. Tenkamp, F. Walther, S. Barcikowski, J. H. Schleifenbaum, B. Gökce, *Procedia CIRP* **2018**, *74*, 196–200.

[41] C. Doñate-Buendía, F. Frömel, M. B. Wilms, R. Streubel, J. Tenkamp, T. Hupfeld, M. Nachev, E. Gökce, A. Weisheit, S. Barcikowski, *Mater. Des.* **2018**, *154*, 360–369.

[42] T. Hupfeld, A. Wegner, M. Blanke, C. Doñate-Buendía, V. Sharov, S. Nieskens, M. Piechotta, M. Giese, S. Barcikowski, B. Gökce, *Adv. Opt. Mater.* **2020**, *8*, 2000473.

[43] T. Hupfeld, S. Salamon, J. Landers, A. Sommereyns, C. Doñate-Buendía, J. Schmidt, H. Wende, M. Schmidt, S. Barcikowski, B. Gökce, *J. Mater. Chem. C* **2020**, *8*, 12204–12217.

[44] A. Kanitz, M. Kalus, E. Gurevich, A. Ostendorf, S. Barcikowski, D. Amans, *Plasma Sources Sci. Technol.* **2019**, *28*, 103001.

[45] R. Tanabe, T. T. Nguyen, T. Sugiura, Y. Ito, *Appl. Surf. Sci.* **2015**, *351*, 327–331.

[46] J. Tomko, J. J. Naddeo, R. Jimenez, Y. Tan, M. Steiner, J. M. Fitz-Gerald, D. M. Bubb, S. M. O'Malley, *Phys. Chem. Chem. Phys.* **2015**, *17*, 16327–16333.

[47] S. Reich, P. Schönfeld, A. Letzel, S. Kohsakowski, M. Olbinado, B. Gökce, S. Barcikowski, A. Plech, *ChemPhysChem* **2017**, *18*, 1084–1090.

[48] S. Ibrahimkutty, P. Wagener, T. dos Santos Rolo, D. Karpov, A. Menzel, T. Baumbach, S. Barcikowski, A. Plech, *Sci. Rep.* **2015**, *5*, 16313.

[49] S. Ibrahimkutty, P. Wagener, A. Menzel, A. Plech, S. Barcikowski, *Appl. Phys. Lett.* **2012**, *101*, 103104.

[50] P. Wagener, S. Ibrahimkutty, A. Menzel, A. Plech, S. Barcikowski, *Phys. Chem. Chem. Phys.* **2013**, *15*, 3068–3074.

[51] S. Reich, A. Letzel, A. Menzel, N. Kretzschmar, B. Gökce, S. Barcikowski, A. Plech, *Nanoscale* **2019**, *11*, 6962–6969.

[52] C.-Y. Shih, R. Streubel, J. Heberle, A. Letzel, M. V. Shugaev, C. Wu, M. Schmidt, B. Gökce, S. Barcikowski, L. V. Zhigilei, *Nanoscale* **2018**, *10*, 6900–6910.

[53] C.-Y. Shih, M. V. Shugaev, C. Wu, L. V. Zhigilei, *Phys. Chem. Chem. Phys.* **2020**, *22*, 7077–7099.

[54] C.-Y. Shih, M. V. Shugaev, C. Wu, L. V. Zhigilei, *J. Phys. Chem. C* **2017**, *121*, 16549–16567.

[55] J. Lam, J. Lombard, C. Dujardin, G. Ledoux, S. Merabia, D. Amans, *Appl. Phys. Lett.* **2016**, *108*, 074104.

[56] H. Qiang, J. Chen, B. Han, Z.-H. Shen, J. Lu, X.-W. Ni, *Opt. express* **2014**, *22*, 17532–17545.

[57] S. Reich, J. Göttlicher, A. Ziefuss, R. Streubel, A. Letzel, A. Menzel, O. Mathon, S. Pascarelli, T. Baumbach, M. Zuber, *Nanoscale* **2020**, *12*, 14011–14020.

[58] A. Letzel, B. Gökce, P. Wagener, S. Ibrahimkutty, A. Menzel, A. Plech, S. Barcikowski, *J. Phys. Chem. C* **2017**, *121*, 5356–5365.

[59] A. Letzel, S. Reich, T. dos Santos Rolo, A. Kanitz, J. Hoppius, A. Rack, M. P. Olbinado, A. Ostendorf, B. Gökce, A. Plech, *Langmuir* **2019**, *35*, 3038–3047.

[60] M.-R. Kalus, N. Bärsch, R. Streubel, E. Gökce, S. Barcikowski, B. Gökce, *Phys. Chem. Chem. Phys.* **2017**, *19*, 7112–7123.

[61] M.-R. Kalus, V. Reimer, S. Barcikowski, B. Gökce, *Appl. Surf. Sci.* **2019**, *465*, 1096–1102.

[62] M.-R. Kalus, R. Lanyumba, N. Lorenzo-Parodi, M. A. Jochmann, K. Kerpen, U. Hagemann, T. C. Schmidt, S. Barcikowski, B. Gökce, *Phys. Chem. Chem. Phys.* **2019**, *21*, 18636–18651.

[63] M.-R. Kalus, R. Lanyumba, N. Lorenzo-Parodi, M. A. Jochmann, K. Kerpen, U. Hagemann, T. C. Schmidt, S. Barcikowski, B. Gökce, *Phys. Chem. Chem. Phys.* **2019**, *21*, 24239.

[64] E. Barmina, A. Simakin, G. Shafeev, *Chem. Phys. Lett.* **2016**, *655*, 35–38.

[65] E. Barmina, A. Simakin, G. Shafeev, *Chem. Phys. Lett.* **2017**, *678*, 192–195.

[66] E. Barmina, S. Gudkov, A. Simakin, G. Shafeev, *J. Laser Micro/Nanoeng.* **2017**, *12*, 254–257.

[67] A. V. Simakin, M. E. Astashev, I. V. Baimler, O. V. Uvarov, V. V. Voronov, M. V. Vedunova, M. A. Sevost'yanov, K. N. Belosludtsev, S. V. Gudkov, *J. Phys. Chem. B* **2019**, *123*, 1869–1880.

[68] A. Schwenke, P. Wagener, S. Nolte, S. Barcikowski, *Appl. Phys. A* **2011**, *104*, 77–82.

[69] A. Baladi, R. S. Mamoory, *Appl. Surf. Sci.* **2010**, *256*, 7559–7564.

[70] Y. Jiang, P. Liu, Y. Liang, H. Li, G. Yang, *Appl. Phys. A* **2011**, *105*, 903–907.

[71] S. Barcikowski, A. Menéndez-Manjón, B. Chichkov, M. Brikas, G. Račiukaitis, *Appl. Phys. Lett.* **2007**, *91*, 083113.

[72] S. Reich, A. Letzel, B. Gökce, A. Menzel, S. Barcikowski, A. Plech, *ChemPhysChem* **2019**, *20*, 1036–1043.

Chemistry–A European Journal

Full Paper
doi.org/10.1002/chem.202005087

Chemistry Europe
European Chemical
Societies Publishing

[73] A. Letzel, M. Santoro, J. Frohleiks, A. R. Ziefuß, S. Reich, A. Plech, E. Fazio, F. Neri, S. Barcikowski, B. Gökce, *Appl. Surf. Sci.* **2019**, *473*, 828–837.

[74] F. Docchio, C. Sacchi, J. Marshall, *Lasers Ophthalmology* **1986**, *1*, 83–93.

[75] P. Ouyang, P. Li, E. Leksina, S. Michurin, L. He, *Appl. Surf. Sci.* **2016**, *360*, 880–888.

[76] S. Nolte, C. Momma, H. Jacobs, A. Tünnermann, B. N. Chichkov, B. Wellegehausen, H. Welling, *J. Opt. Soc. Am. B.* **1997**, *14*, 2716–2722.

[77] M. Shaheen, J. Gagnon, B. Fryer, *J. Appl. Phys.* **2013**, *114*, 083110.

[78] N. Semaltianos, W. Perrie, P. French, M. Sharp, G. Dearden, S. Logothetidis, K. Watkins, *Appl. Phys. A* **2009**, *94*, 999–1009.

[79] M. Shaheen, J. Gagnon, B. Fryer, *Laser Phys.* **2014**, *24*, 106102.

[80] J. Güdde, J. Hohlfeld, J. Müller, E. Matthias, *Appl. Surf. Sci.* **1998**, *127*, 40–45.

[81] N. Lasemi, U. Pacher, L. Zhigilei, O. Bomatí-Miguel, R. Lahoz, W. Kautek, *Appl. Surf. Sci.* **2018**, *433*, 772–779.

[82] S. V. Starinskiy, Y. G. Shukhov, A. V. Bulgakov, *Appl. Surf. Sci.* **2017**, *396*, 1765–1774.

[83] H. Mustafa, M. Mezera, D. T. A. Matthews, G. Römer, *Appl. Surf. Sci.* **2019**, *488*, 10–21.

[84] O. Benavides, L. de la Cruz May, E. Mejia, J. R. Hernandez, A. F. Gil, *Laser Phys.* **2016**, *26*, 126101.

[85] J. A. Dean, *Lange's Handbook of Chemistry*, McGraw-Hill Inc., New York, **1999**.

[86] E. György, I. Mihailescu, P. Serra, A. P. Del Pino, J. Morenza, *Surf. Coat. Technol.* **2002**, *154*, 63–67.

[87] D. Perez, L. J. Lewis, P. Lorazo, M. Meunier, *Appl. Phys. Lett.* **2006**, *89*, 141907.

[88] R. Karimzadeh, J. Z. Anvari, N. Mansour, *Appl. Phys. A* **2009**, *94*, 949–955.

[89] K. Boboridis, G. Pottlacher, H. Jäger, *Int. J. Thermophys.* **1999**, *20*, 1289–1297.

[90] V. Morel, A. Bultel, B. Chéron, *Int. J. Thermophys.* **2009**, *30*, 1853.

[91] A. L. Khomkin, A. S. Shumikhin, *High Temp. High Pressures* **2016**, *56*, 367–376.

[92] S. V. Starinskiy, A. A. Rodionov, Y. G. Shukhov, E. A. Maximovskiy, A. V. Bulgakov, *Appl. Phys. A* **2019**, *125*, 734.

[93] A. Tamura, A. Matsumoto, K. Fukami, N. Nishi, T. Sakka, *J. Appl. Phys.* **2015**, *117*, 173304.

[94] T. Hupfeld, G. Laurens, S. Merabia, S. Barcikowski, B. Gökce, D. Amans, *J. Appl. Phys.* **2020**, *127*, 044306.

[95] C.-Y. Shih, I. Gnilitskyi, M. V. Shugaev, E. Skoulas, E. Stratakis, L. V. Zhigilei, *Nanoscale* **2020**, *12*, 7674–7687.

[96] M. Domke, S. Rapp, M. Schmidt, H. P. Huber, *Opt. express* **2012**, *20*, 10330–10338.

[97] S. Rapp, M. Kaiser, M. Schmidt, H. P. Huber, *Opt. express* **2016**, *24*, 17572–17592.

[98] S. Reich, J. Göttlicher, A. Letzel, B. Gökce, S. Barcikowski, T. dos Santos Rolo, T. Baumbach, A. Plech, *Appl. Phys. A* **2018**, *124*, 71.

[99] R. David, *CRC Handbook of Chemistry and Physics* CRC Press, Florida, **2009**.

[100] J. Krüger, W. Kautek, *Ultrashort pulse laser interaction with dielectrics and polymers*, Springer, Berlin, **2004**.

[101] B. N. Chichkov, C. Momma, S. Nolte, F. Von Alvensleben, A. Tünnermann, *Appl. Phys. A* **1996**, *63*, 109–115.

[102] C. Momma, B. N. Chichkov, S. Nolte, F. von Alvensleben, A. Tünnermann, H. Welling, B. Wellegehausen, *Opt. Commun.* **1996**, *129*, 134–142.

[103] R. Lahoz, A. Naghilou, W. Kautek, O. Bomati-Miguel, *Appl. Surf. Sci.* **2020**, *511*, 145438.

[104] B. Kumar, R. K. Thareja, *Phys. Plasmas* **2012**, *19*, 033516.

[105] D. Amans, M. Diouf, J. Lam, G. Ledoux, C. Dujardin, *J. Colloid Interface Sci.* **2017**, *489*, 114–125.

[106] S. Barcikowski, A. Plech, K. S. Suslick, A. Vogel, *MRS Bull.* **2019**, *44*, 382–391.

[107] S. Jendrzej, B. Gökce, V. Amendola, S. Barcikowski, *J. Colloid Interface Sci.* **2016**, *463*, 299–307.